Conserved Functions of Ether Lipids and Sphingolipids in the Early Secretory Pathway

Noemi Jiménez-Rojo,[1,8] Manuel D. Leonetti,[2,3,7,8] Valeria Zoni,[4] Adai Colom,[1] Suihan Feng,[1] Namrata R. Iyengar,[5] Stefan Matile,[6] Aurélien Roux,[1] Stefano Vanni,[4] Jonathan S. Weissman,[2,3] and Howard Riezman[1,9,*]

[1]NCCR Chemical Biology, Department of Biochemistry, University of Geneva, 1211 Geneva, Switzerland
[2]Department of Cellular and Molecular Pharmacology, University of California, San Francisco, San Francisco, CA 94158, USA
[3]Howard Hughes Medical Institute, San Francisco, CA 94158, USA
[4]Department of Biology, University of Fribourg, Fribourg, Switzerland
[5]Institute of Protein Biochemistry (IBP), Italian National Research Council (CNR), Napoli, Italy
[6]NCCR Chemical Biology, Department of Organic Chemistry, University of Geneva, 1211 Geneva, Switzerland
[7]Present address: Chan Zuckerberg Biohub, San Francisco, CA 94158, USA
[8]These authors contributed equally
[9]Lead Contact
*Correspondence: howard.riezman@unige.ch

SUMMARY

Sphingolipids play important roles in physiology and cell biology, but a systematic examination of their functions is lacking. We performed a genome-wide CRISPRi screen in sphingolipid-depleted human cells and identified hypersensitive mutants in genes of membrane trafficking and lipid biosynthesis, including ether lipid synthesis. Systematic lipidomic analysis showed a coordinate regulation of ether lipids with sphingolipids, suggesting an adaptation and functional compensation. Biophysical experiments on model membranes show common properties of these structurally diverse lipids that also share a known function as glycosylphosphatidylinositol (GPI) anchors in different kingdoms of life. Molecular dynamics simulations show a selective enrichment of ether phosphatidylcholine around p24 proteins, which are receptors for the export of GPI-anchored proteins and have been shown to bind a specific sphingomyelin species. Our results support a model of convergent evolution of proteins and lipids, based on their physico-chemical properties, to regulate GPI-anchored protein transport and maintain homeostasis in the early secretory pathway.
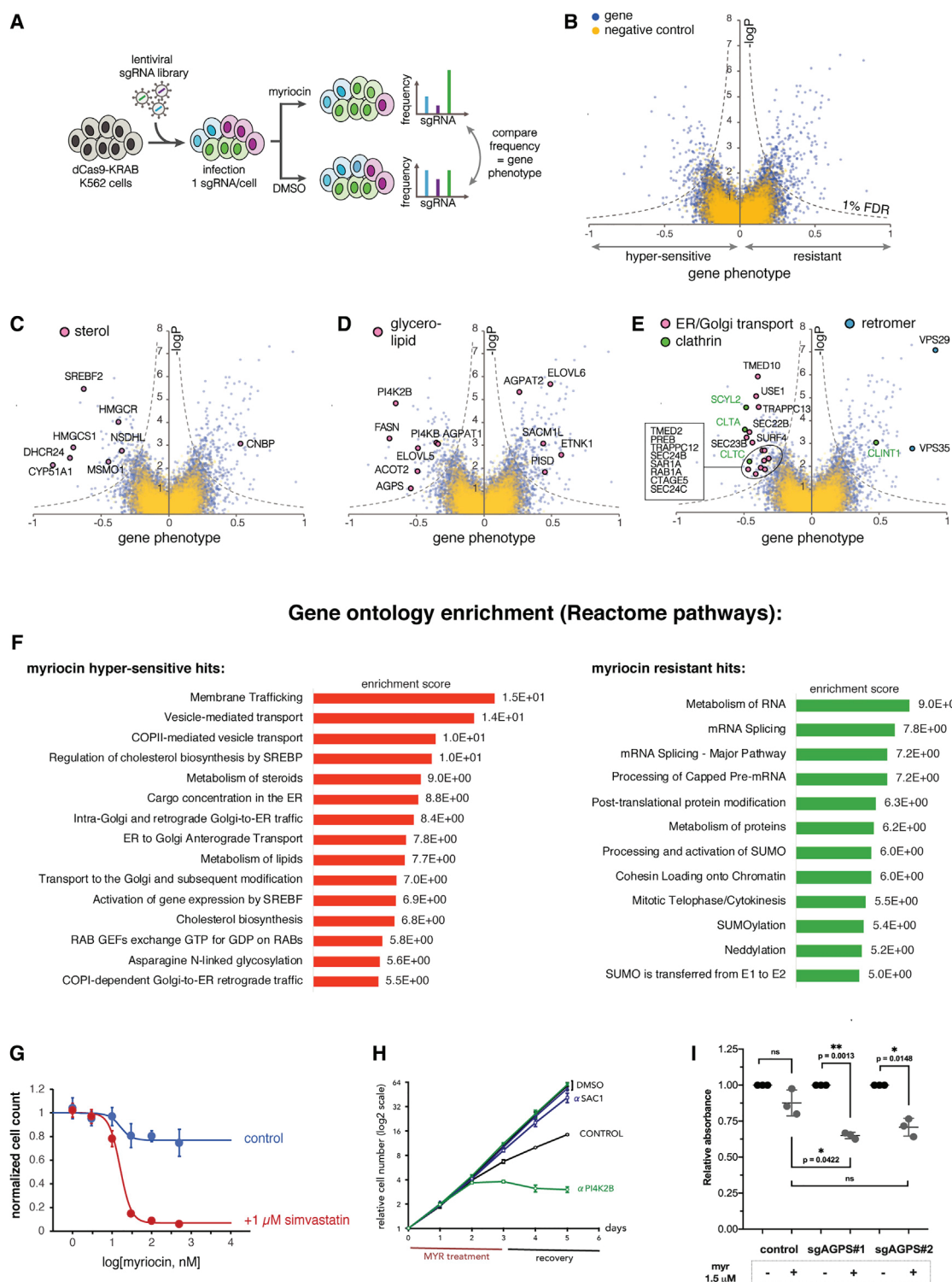
INTRODUCTION

The maintenance of membrane lipid homeostasis is an energetically expensive yet necessary process in cells. Lipid diversity has evolved together with cell complexity to give rise to thousands of different lipids species with specific functions, many of which are still unexplored [1, 2]. Moreover, different lipid metabolic pathways are interconnected, and cells show a high phenotypic plasticity when adapting to changes in membrane lipid composition, which makes it difficult to disentangle the function of individual lipid species [3]. A systematic analysis of the cellular responses to perturbation of specific synthetic pathways is thus needed to reveal co-regulated lipid networks and uncover new lipid functions.

Sphingolipids (SLs) are a class of lipids that contain a sphingoid-base backbone, in contrast to the more commonly found glycerol backbone in glycerophospholipids (GPLs). These bioactive lipids have been extensively studied in the last decades, revealing distinctive physico-chemical properties and connections to diseases [4, 5]. SLs have been implicated in diabetes [6], cancer [7], and inflammation [8], and mutations in SL synthetic or metabolic enzymes are associated with severe genetic

disorders [9–11]. SL species sphingosine (So) and ceramide (Cer) can permeabilize membranes [12, 13]; Cer induces the flip-flop of neighboring lipids [14] and can phase separate to form membrane platforms important for signaling [15]. The most abundant SL species, sphingomyelin (SM), has been shown to modulate membrane properties and regulate signaling pathways [16, 17]. Besides direct phosphorylation of Cer synthases [18–20], the only direct regulators of SL synthesis identified are Orm proteins (ORMDL in mammalian cells), which associate with serine palmitoyl transferase (SPT), the first enzyme of the SL de novo synthetic pathway, and mediate the feedback regulation of SL production in cells [21, 22]. Despite this body of work, many basic aspects of the regulation, molecular interactors, and functions of SL still remain poorly understood.

Ether lipids (ELs) form a poorly characterized lipid family that represents a subclass of GPLs that are defined by the presence of an ether bond (or vinyl ether for plasmalogens) in lieu of the ester bond found in canonical phospholipids at the sn-1 position. This feature, which is intermittently represented across the evolutionary tree, is decisive for the behavior of these lipids in membranes and for specific lipid-protein interactions [23]. Interestingly, ELs are not only present in membranes as abundant

Figure 1. A Genetic Screen in Sphingolipid-Depleted Cells Highlights Lipid Co-dependencies and Uncovers a Major Role for Sphingolipids in Intracellular Transport

(A) Schematic of myriocin sensitivity CRISPRi screen in K562 cells.

(B) Volcano plot showing gene phenotype on the x axis and logP value on the y axis. Each dot is an individual gene (blue). Negative control phenotypes reconstructed from non-targeting sgRNAs are shown in yellow.

(C) Hits that include genes involved in sterol metabolism.

(D) Hits involved in membrane lipid metabolism.

2

lipid components, where they can range from approximately 5–20 mol % of the total GPL content, but are also a major building block of glycosylphosphatidylinositol (GPI) anchors, a specialized protein post-translational modification. Peroxisomal synthesis of EL is necessary for the synthesis of the 1-alkyl, 2-acyl phosphatidylinositol GPI anchor, which is attached to most of the mammalian GPI-anchored proteins (GPI-AP) in the endoplasmic reticulum (ER) [24, 25]. GPI-AP are then exported (through binding to p24 proteins: TMED2 and TMED10 in human) from the ER to the plasma membrane via the Golgi complex, where they undergo different remodeling modifications, replacing the unsaturated fatty acid in the sn-2 position with a saturated one. Interestingly, the same p24 proteins that selectively pack GPI-AP into the COPII carriers [26, 27] are also involved in COPI-dependent retrograde transport [28, 29], through the binding of a particular SM species (SM C18 n-acyl) that regulates the initiation of COPI vesicle budding and retrograde transport from the Golgi to the ER [30].

Here, we apply high-throughput genetics and lipidomic methods to uncover novel regulatory aspects of SL metabolism, and we find a co-regulation of this lipid class with the structurally unrelated EL. Our multidisciplinary approach combining molecular dynamics (MD) simulations with the study of GPI-AP transport kinetics establishes an active role for (ether)lipids in the transport of GPI-AP from the ER to the Golgi and emphasizes the physico-chemical properties of EL that enabled them to be selected in mammalian cells to perform this function.

RESULTS AND DISCUSSION

A Genetic Screen in SL-Depleted Cells Highlights Lipid Co-dependencies and Uncovers a Major Role for SLs in Intracellular Transport

To identify pathways regulating cellular responses to SL depletion, we performed a genome-wide CRISPRi growth screen for genes that modulate sensitivity to myriocin, an inhibitor of *de novo* SL synthesis. To ensure dependence on *de novo* lipid synthesis (as opposed to exogenous lipid intake, which can circumvent the need for cellular synthesis) [31], we cultured human K562 cells in lipid-depleted serum (see STAR Methods). Indeed, we found that myriocin treatment efficiently arrested growth in lipid-depleted media, but not in lipid-rich media, and lipid depletion alone did not compromise growth (Figure S1A). Lipidomic analysis verified that myriocin treatment severely decreased

cellular SL levels (Figures 2A, 2B, S1B, and S1C) under these conditions.

To systematically repress gene expression, we used an ultra-complex genome-wide CRISPRi library targeting 15,977 genes using 10 sgRNAs (single guide RNAs) per gene [32], also including 1,000 non-targeting control sgRNAs to allow precise measurement of experimental noise. For screening, K562 cells stably expressing dCas9-KRAB were infected with a pooled lentiviral library of sgRNA constructs, and dCas9/sgRNA-expressing cells were treated with myriocin or DMSO in lipid-depleted media (Figure 1A). Deep sequencing analysis using sgRNA sequences as barcodes [32, 33] revealed the impact of individual gene knockdown on survival under SL restriction. Screening analysis revealed a rich dataset, with over 450 genes regulating survival under myriocin treatment (Figure 1B; Data S1). Strikingly, several gene families emerged with strong phenotypes, linking survival under SL depletion to other lipid synthetic pathways and intracellular vesicular transport, in particular. Indeed, when Gene Ontology (GO) enrichment is used, hypersensitive hits are enriched in ER-Golgi transport, sterol metabolism, membrane trafficking, and lipid synthesis, although resistant pathways are harder to define: mRNA regulation and post-translational modifications, suggesting more complex pathways that remain to be understood.

First, repression of sterol synthesis enzymes or their transcriptional activator SREBF2 strongly compromised the ability of cells to survive without SL (Figure 1C). We further verified this strong co-dependency between SL and sterols by showing that sterol synthesis inhibition with simvastatin greatly accentuates the impact of myriocin on growth (Figure 1G). This highlights the synergistic function of SLs and sterols, which has been previously described in yeast by Guan et al. [34], where the authors found correlative changes in sterol and SL homeostasis and synthetic phenotypes between different sterol and SL mutants, demonstrating that sterols and SLs work together in biological membranes. Interestingly, cells lacking CNBP (cellular nucleic-acid-binding protein), a poorly characterized zinc-finger protein linked to repression of SREBP targets [35], appear as resistant to myriocin treatment in our dataset, in agreement with its potential antagonistic role.

Second, perturbations of different routes of GPL metabolism and remodeling showed both aggravating and resistant phenotypes (Figure 1D), indicating a functional crosstalk between SL and specific GPL species. Interestingly, specific pathways for acyl chain remodeling showed either resistance

(E) Hits involved in intracellular transport, including those involved in the early secretory pathway and clathrin-mediated trafficking.
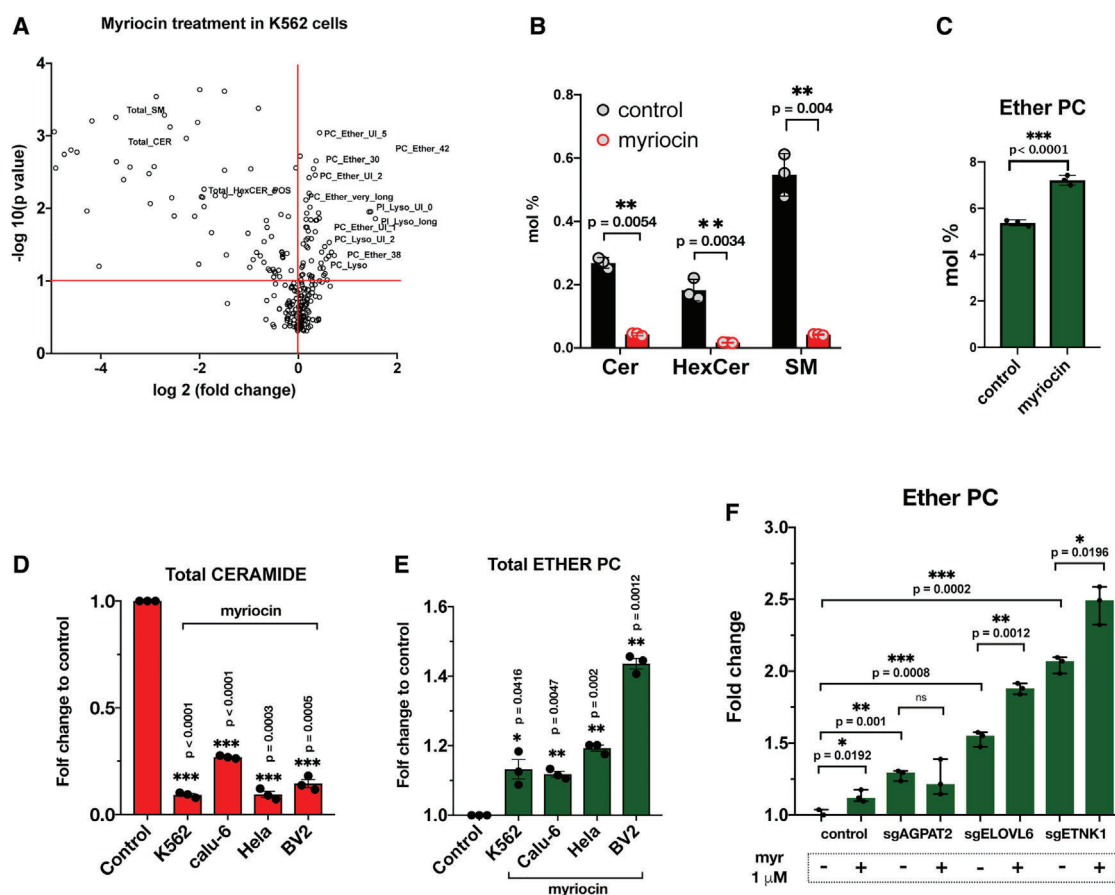(F) Pathway analysis of CRISPRi screen. Gene lists from hypersensitive or resistant myriocin hits were subjected to gene ontology analysis (pathway annotations from Reactome version 65). Enrichment scores ($-$log p value of enrichment) were calculated with PANTHER using the whole human genome as reference set. Shown are pathways with enrichment $p < 10^{-5}$.
(G) Myriocin dose-response curves showing K562 cell survival in the absence (control) or presence of 1 μM simvastatin after 3 days of treatment in de-lipidated media. Each point represents average ± standard deviation from 3 independent measurements (some error bars are smaller than symbols). Sigmoid fits (solid lines) with IC_{50} (half maximal inhibitory concentration) = 16 nM are shown.
(H) Myriocin sensitivity of CRISPRi K562 dCas9-Krab lines. Growth curves are shown for parental line (no sgRNA; "control"), SACM1L knockdown (aSAC1), and PI4K2B knockdown (aPI4K2B). Note that cell count (y axis) is shown on a log2 scale. Open symbols: growth upon 3-day treatment with 1 μM myriocin, followed by 3 days of recovery, is shown. Full symbols: un-treated controls (DMSO) are shown. SACM1L knockdown protects from the growth impact of myriocin, although PI4K2B knockdown accentuates its effect. Shown are average and standard deviation from 3 independent replicate experiments.
(I) Myriocin sensitivity of ether lipid-depleted HeLa CRISPRi cell lines using the colorimetric MTT assay. Data were normalized to control for each condition (vehicle). Each data point represents the average absorbance in one well.
See also Figure S1 and Data S1.

Figure 2. Systematic Lipidomic Analysis Reveals a Metabolic Co-regulation of Sphingolipids and Ether Lipids

(A) Lipid changes in K562 cells after 3-day inhibition of sphingolipid synthesis with 1 μM myriocin. Log 2 of the fold change compared to control cells in the x axis and the −log p value in the y axis (n = 3) are shown.

(B) Relative sphingolipid species amount over the total of lipids detected (n = 3). Cer, total ceramide; HexCer, total hexacylceramide; SM, total sphingomyelin.

(C) Relative ether phosphatidylcholine (PC) levels (n = 3).

(D) Decrease in ceramide levels upon myriocin treatment in different cell lines (n = 3).

(E) Increase in ether PC levels upon myriocin treatment in different cell lines (n = 3).

(F) Relative ether PC levels in myriocin-resistant cell lines before and after treatment (n = 3).

Each condition represents the mean of 3 independent measurements of approximately 2 million cells. Statistical analysis was performed by unpaired two-tailed Student's t test. See also Figures S1 and S2 and Data S2 and S3.

or hypersensitivity to SL depletion (ELOVL5/6 and AGPAT1/2). In particular, repression of ELOVL5, an enzyme with specificity to elongate polyunsaturated fatty acids (PUFAs), is hypersensitive, although ELOVL6, which has specificity to elongate saturated C16 acyl coenzymes A (CoAs) is a resistant hit, showing that acyl chain saturation can modulate survival in the absence of SL synthesis. Our results also highlighted a strong interaction between SL and phosphatidylinositol-4-phosphate (PI4P) synthesis. Indeed, repression of PI4 kinases (PI4K and PI4K2B) strongly compromised growth although repression of the PI4P-phosphatase SACM1L (SAC1) allowed survival upon SL depletion. This striking signature was verified in individual follow-up experiments (Figure 1H) and mirrors previous results in *S. cerevisiae*, where Sac1 knockout renders yeast resistant to myriocin [21], suggesting that the link between SL and PI4P homeostasis has been conserved during evolution. Indeed, SLs have also been shown to regulate phosphoinositide turnover at the Golgi in

mammalian cells, and the metabolic coupling of PI4 kinases/ Sac1 phosphatase seems to be responsible for the control of phosphoinositide phosphate (PtdIns(4)P) amounts in response to SL levels in the Golgi [36].

Interestingly, inhibition of ether lipid synthesis through repression of alkyldihydroxyacetonephosphate synthase (AGPS), a peroxisomal enzyme responsible for the first ether-linked precursor in EL synthesis, also compromised survival to myriocin treatment. This functional interaction was confirmed in another cell line: AGPS knockdown in CRISPRi HeLa cells using two sgRNAs also displayed myriocin hypersensitivity (Figure 1I). The first guide RNA (sgAGPS 1) was used for further experiments throughout the paper, as it showed the best knockdown efficiency and the strongest decrease in ether lipid levels (Figures S1E and S1F). Altogether, our genetic screen revealed rich functional crosstalks between SL and a variety of other lipid species (in particular, sterols, PI4P, and EL).

Finally, SL-depleted cells were particularly vulnerable to inhibition of intracellular vesicular transport (Figure 1E). Specifically, many members of the COPII machinery (responsible for ER to Golgi transport), including coat proteins (PREB [SEC12], SAR1, SEC24B/C, and SEC23B), cargo receptors (TMED2 and TMED10), and proteins involved in the docking and fusion of the carriers (RAB1A, SEC22B, and USE1) were strong hypersensitive hits, as were key proteins in clathrin-mediated transport (CLTA, CLTC, and SCYL2). SCYL2 has been proposed to regulate clathrin-mediated transport from TGN (trans-Golgi network) to endosomes [37], suggesting that maintenance of SL levels is specifically important for traffic through the secretory pathway. Some of these hits raise new questions in the SL and membrane trafficking fields. For instance, cells lacking SURF4, a protein affecting ER morphology, are hypersensitive to myriocin, as well as cells knocked down for cTAGE5, a protein involved in the ER to Golgi transport of large cargos, such as collagen [38]. Elucidating the mechanism by which SLs regulate secretion of large cargos could be of interest to understand collagen-related diseases among others [39, 40]. Alternatively, cells lacking components of the retromer complex (VPS29 and VPS35) appear as resistant to SL depletion (Figure 1E). Again, these phenotypes open new possibilities for lipid-dependent cargo sorting in endosomal trafficking, which merit further investigation.

Systematic Lipidomic Analysis Reveals a Metabolic Co-regulation of SLs and Ether Lipids

Because our screen revealed strong functional interplays between SL levels and other steps in lipid metabolism, we decided to combine the genetic data with lipidomic analysis to identify co-regulated lipid species and new lipid functions. This analysis highlighted a pronounced crosstalk between SL and EL levels. First, when profiling the lipidome of SL-depleted cells after myriocin treatment, we detected a consistent increase in EL, in particular ether phosphatidylcholine (PC) species (Figures 2A, 2C, S1B, and S1D). Indeed, we could see this metabolic response in cell lines from different tissues, showing a conserved response including mouse and human cell lines (Figures 2D and 2E) but showing no obvious correlation between the amplitude of the decrease in SL levels and the increase in ether PC levels. Furthermore, lipidomic analysis of some of the resistant hits from the CRISPRi screen (Figure 1D) showed that they had higher amounts of ether PC in comparison with control cells (Figure 2F), suggesting that having increased baseline levels of EL can make cells resistant to SL depletion.

Overall, these results show a co-regulation between the levels of EL and SL in mammalian cells that can explain the genetic interaction seen in our myriocin screen. This prompted us to investigate whether the response of cells to increased ether lipid levels upon SL depletion was bidirectional. For that purpose, we used AGPS knockdown cells and analyzed their lipidome to see whether those cells, depleted of EL, showed changes in SL levels (Figures 3A–3G). Indeed, under these conditions, the total amount of Cer was increased around 20%, driven by increases in a wide range (C16, C18, C22, and C24) of Cer species (Figure 3D), although hexosylceramide (HexCer) levels were unchanged (Figure 3C). Moreover, even though the total amount of SM and the levels of the major SM (SM C24:1) were not affected, we found a decrease in specific SM species, SM with a C18 n-acyl chain (Figures 3E and 3F).
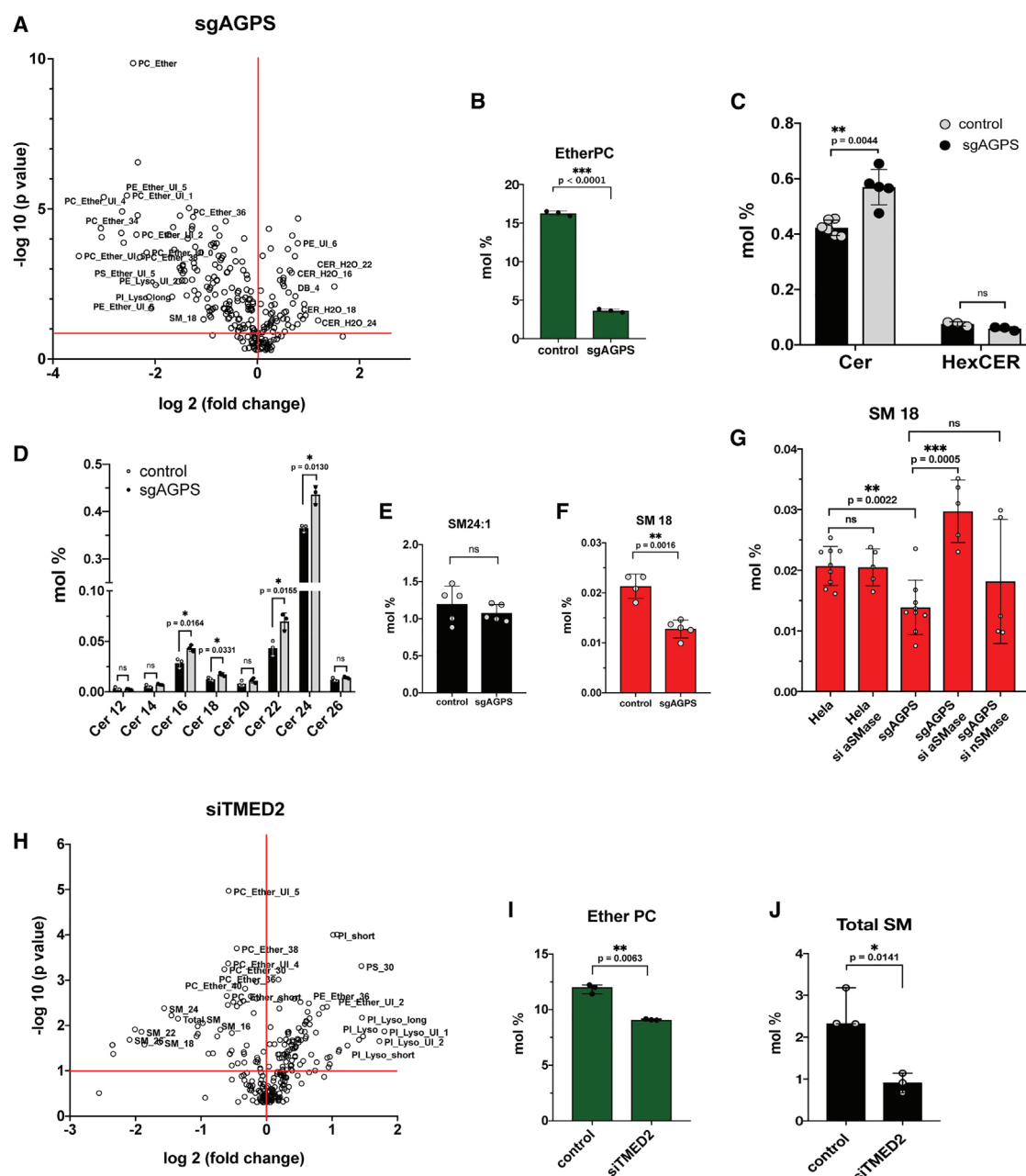
A unifying interpretation of these lipid changes suggested a possible role of EL in the early secretory pathway. First, this specific SM (SM C18) has been shown to be important for an efficient COPI-dependent retrograde transport from Golgi to the ER through specific binding to p24 proteins [30], receptors for the export of GPI-AP in the anterograde pathway [27]. Second, we find some components of the p24 complex as hypersensitive in the myriocin screen (TMED2 and TMED10; Figure 1E), and cells lacking TMED2 show a decrease in the levels of both EL and SM (Figures 3H–3J), which shows that the levels of these lipids respond to defects in the secretory pathway. The decrease in EL levels upon TMED2 knockdown (KD) could be due to a possible role for these proteins in peroxisomal function, as they have been described to be present in peroxisomes in yeast cells [41]. Another possibility could be that the accumulation of ether-lipid-containing GPI-AP in the ER signals through a feedback loop to decrease the synthesis of ether lipids. Either hypothesis predicts a close link between p24 protein function and lipid metabolism and warrant further investigation. Finally, the perturbed Golgi structure upon TMED2 KD could be at the origin of the observed decrease in SM (Figure S4M).

The specific effect on SM C18 upon ether lipid depletion is remarkable. It is possible that changes in the levels of SM C18 could be used as an indicator of defects in COPI-dependent retrograde transport and that, when retrograde transport is reduced, SM C18 is redirected to the endosomal-lysosomal pathway. To test this, we attempted to rescue the decrease in SM C18 levels in AGPS KD cells by knocking down the acid sphingomyelinase (aSMase), which is located in the lysosome (Figure 3G). Indeed, reducing aSMase, but not the neutral sphingomyelinase, restored levels of SM C18, consistent with SM C18 being redirected toward lysosomes.

It is also worth mentioning that lysolipids seem to be affected in all of the analyzed conditions. They increase both when SLs are depleted, when TMED2 is inactivated, and they are decreased when ELs are depleted. Because we previously showed that lysolipids can facilitate COPII vesicle formation [42], we believe their levels could respond to altered kinetics of the secretory pathway, although the precise mechanism still needs to be described in mammalian cells.

Similar Effects of Cer and Ether Lipids on Membrane Organization

The genetic interaction seen between EL and SL metabolism in the screening and the bidirectional co-regulation found in our lipidomics data between Cer and ether PC indicated that, even though these lipids are very different in terms of their chemical structure, they might share functions in cell membranes. Indeed, one common function, apparent from different kingdoms of life, is as part of the lipid anchor in GPI-AP. In yeast, the plasma membrane GPI-AP often has a Cer-based anchor [43], although in mammalian cells, most have an ether-lipid-based anchor [44]. Therefore, we speculated that SLs and ELs could share functions in the secretory pathway and that their selection for this function could be based on their physico-chemical properties and behavior in membranes.

Figure 3. Lipidomic Analysis of Ether-Lipid-Deficient Cells Confirms the Crosstalk between Sphingolipids and Ether Lipids

(A) Lipid changes in ether lipid-deficient HeLa cells where alkyldihydroxyacetonephosphate synthase (AGPS) has been knocked down using CRISPRi. Log 2 of the fold change compared to control cells in the x axis and the −log p value in the y axis are shown.

(B) Relative ether PC levels over the total of lipids detected (n = 3).

(C) Relative ceramide and hexosylceramide levels over the total of lipids detected. Cer, total ceramide (n = 5); HexCer, total hexosylceramide (n = 5).

(D) Relative SM 24:1 levels over the total of lipids detected (n = 5).

(E) Relative SM C18 levels over the total of lipids detected (n = 5).

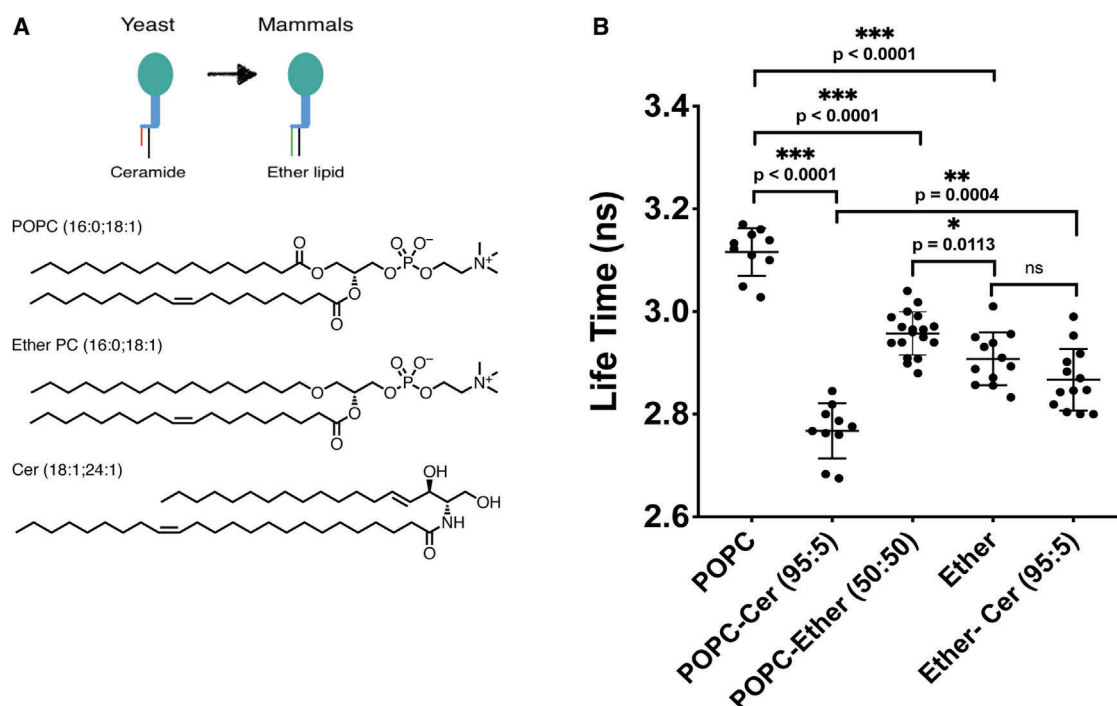(F) Ceramide profile of ether-lipid-depleted cells (n = 3).

(G) Relative SM C18 levels in ether-lipid-deficient cells are rescued by the knockdown of the lysosome-localized acid sphingomyelinase (aSMase) (SMPD1), but not by the neutral sphingomyelinase (nSMase) (SMPD3). Cells were transfected with small interfering RNA (siRNA) for 3 days and then analyzed by tandem mass spectrometry.

(H) Lipid changes in p24 (TMED2) knockdown HeLa cells. Log 2 of the fold change compared to control cells in the x axis and the −log p value in the y axis are shown.

(I) Relative ether PC levels in p24 (TMED2) knocked down cells (n = 3).

(J) Relative SM levels in p24 (TMED2) knocked down cells (n = 3).

See also Figure S2 and Data S2 and S3.

6

Figure 4. Similar Effects of Ceramide and Ether Lipids on Membrane Organization

(A) Upper panel: schematic representation of GPI-AP structure in yeast (ceramide-based anchor) and in mammalian cells (ether-lipid-based anchor). Lower panel: structure of the lipids used for this study is shown. Cer 24:1, N-nervonoyl-D-erythro-sphingosine; ether PC, 1-O-hexadecyl-2-oleoyl-sn glycero-3-phosphocholine; POPC, 1-palmitoyl-2-oleoyl-glycero-3-phosphocholine.

(B) Fluorescence lifetime values of the FLIPPER-TR probe as a function of lipid composition in giant unilamellar vesicles. GUVs were composed of either POPC or ether PC and binary mixtures of POPC + 5% ceramide 24:1 and ether PC + 5% ceramide 24:1 as well as an equimolar mixture of POPC and ether PC.

See also Figure S3.

To investigate this, we used a simplified system and reconstituted bilayers composed of ether PC or Cer in combination with 1-palmitoyl-2-oleoyl-glycero-3-phosphocholine (POPC) that we used as a model "scaffold" for the ER membrane (Figure 4A). To probe lipid packing of these giant unilamellar vesicles (GUVs), we used a mechanosensitive membrane probe (FLIPPER-TR) recently described to measure membrane tension and lipid packing [45, 46]. Both ether PC and Cer (at 5 mol % of Cer 24:1 where microscopic phase separation was not detectable) showed similar behavior, decreasing the lifetime of the FLIPPER-TR probe when present in GUVs composed of POPC (Figure 4B). Ether PC alone showed an even more marked decrease in the fluorescence lifetime of the probe. Interestingly, Cer had no effect when present in GUVs composed of ether PC (Figure 4B). This difference in behavior could be explained by a differential interaction of Cer molecules with ether PC compared to POPC, a hypothesis that is supported by a slight decrease in the amount of hydrogen bonds that Cer forms with ether PC compared to POPC (Figure S3B). Thus, even though they are not microscopically visible with this lipid composition, both Cer 24:1 and ether PC could form nanoscopic packing defects in POPC membranes, and the lipid decompression in those areas would be detected as a decrease in fluorescent lifetime of the probe due to a deplanarization of the FLIPPER-TR molecule [45]. As expected, even though they change the lifetime in the sam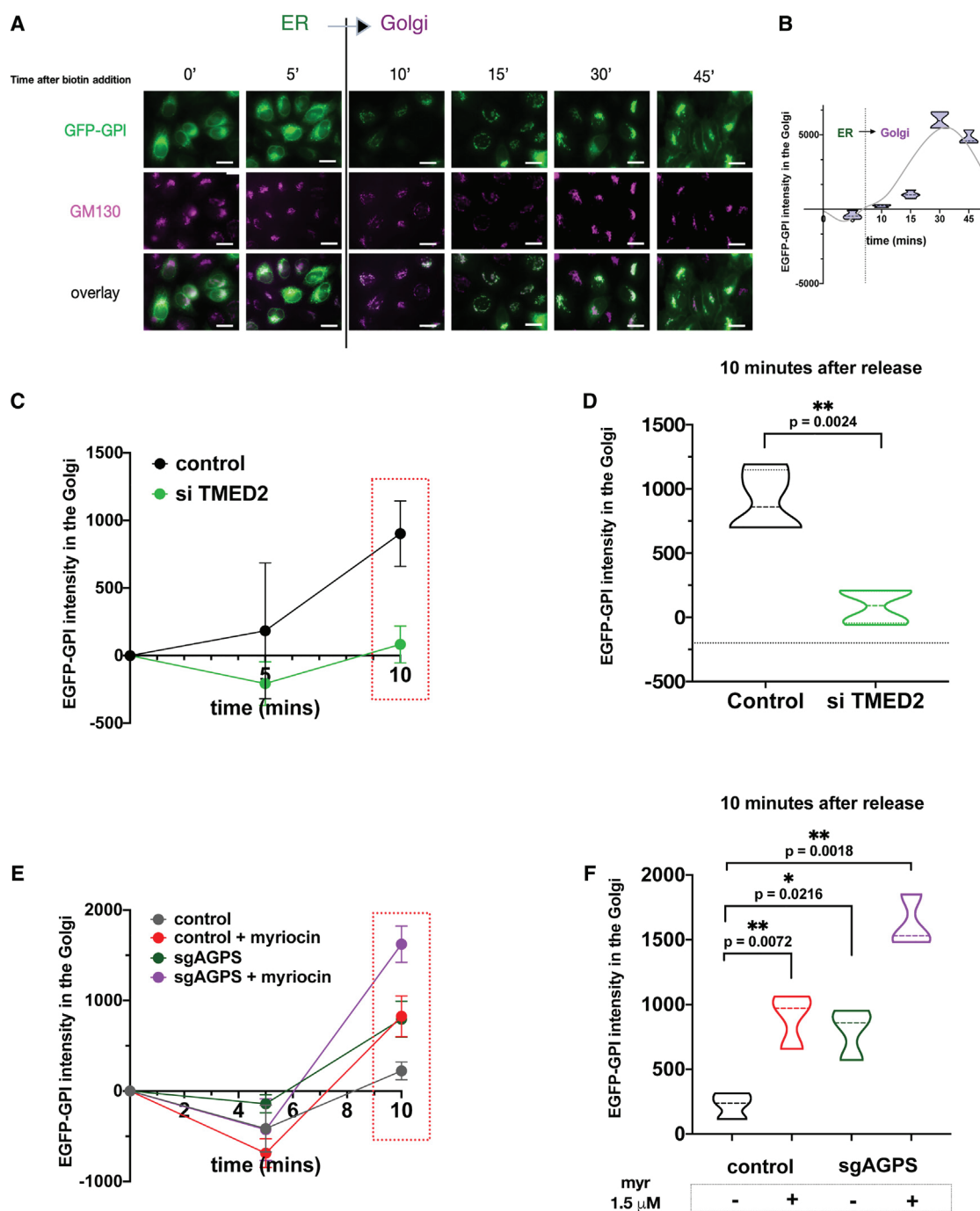e direction, the addition of 5% Cer24:1 induces a more drastic effect on membrane structure than the addition of the same amount of ether PC to vesicles composed of POPC (Figure S3A). This is probably pertinent to the *in vivo* situation, because ether PC is more abundant than Cer24:1.

This interpretation of lipid co-regulation to achieve specific properties/functions is not only applicable to particular cells or tissues but should also be considered through evolution, where different organisms have different lipid compositions, even though they often need to perform similar tasks. A high amount of lipid diversity should be an evolutionary advantage in this respect.

Ether Lipid Depletion Accelerates Anterograde Transport of GPI-Anchored Proteins

It is possible that adaptation of lipid composition is a strategy the cells use to modulate the kinetics of export of proteins from the ER and that ELs and SLs are at the center of this regulatory hub. In order to examine this, we took advantage of the RUSH system (retention using selective hooks), a technique to synchronize ER export of cargo proteins by addition of biotin, [47] to investigate the export of GPI-AP under different conditions.

To monitor arrival of secreted proteins to the Golgi, we used fluorescence microscopy and quantified the GFP signal from an EGFP-GPI construct in the Golgi, which was segmented from images of cells where the *cis*-Golgi was stained using an anti-GM130 antibody (Figures 5A, 5B, and S4). Because of

Figure 5. Ether Lipid Depletion Accelerates Anterograde Transport of GPI-Anchored Proteins

(A) Representative images of the RUSH assay in control cells (0, 5, 10, 15, 30, and 45 min after release) and p24 knockdown cells (10 min after release). The transfected cargo (EGFP-GPI) is released from the ER upon biotin addition and transported to the Golgi apparatus. Scale bars, 20 μm.

(B) Representative quantification of the RUSH assay in control cells 45 min after biotin addition.

(C) Kinetics of the export of GPI-anchored proteins upon TMED2 knockdown 10 min after biotin addition.
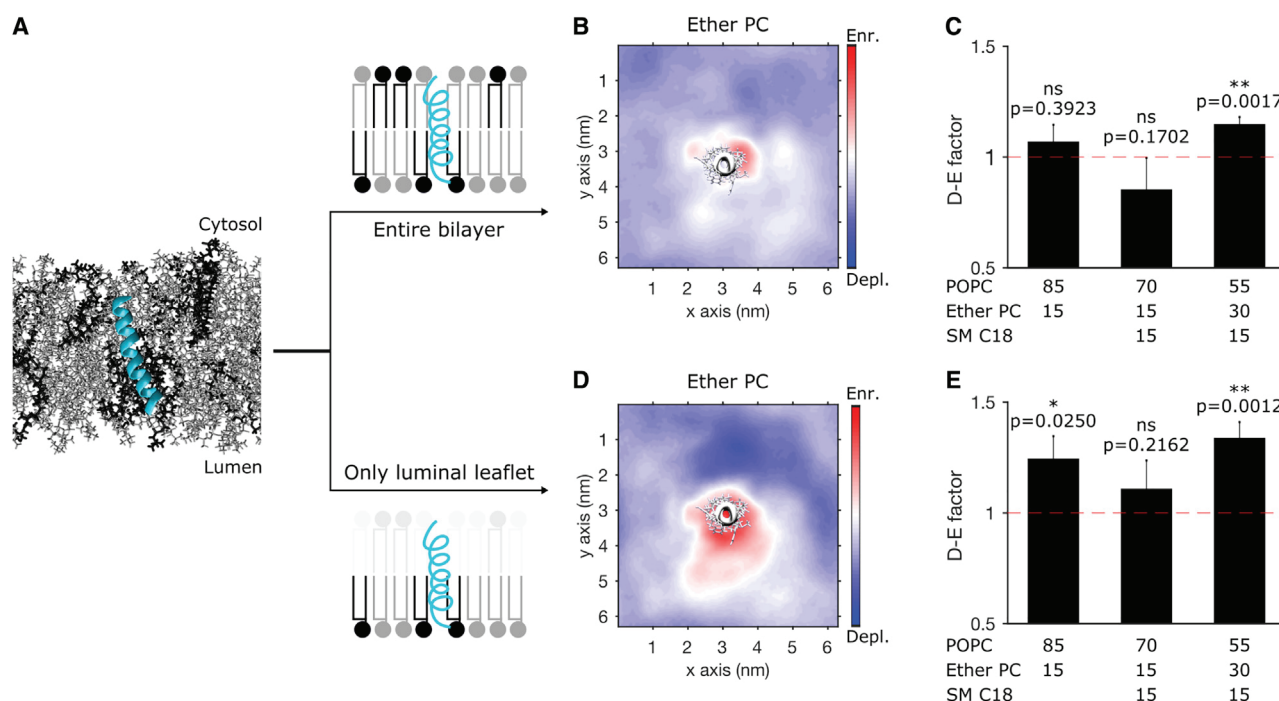
(D) Quantification of the fluorescence intensity of the transfected cargo in the Golgi 10 min after biotin addition (control n = 540 cells; TMED2 knockdown n = 1,555 cells).

(E) Kinetics of the export of GPI-anchored proteins when cells were treated with myriocin or/and when AGPS was knocked down.

(F) Quantification of the fluorescence intensity of the transfected cargo in the Golgi 10 min after biotin addition (control: n = 2,198 cells; myriocin: n = 1,984 cells; sgAGPS: n = 2,441 cells; sgAGPS + myriocin: n = 1,398 cells).

See also Figure S4.

Figure 6. Ether PC Interacts with the Luminal Leaflet of p24 TMD

(A) Snapshot from MD simulations of p24 TMD (cyan) in a POPC (gray) and EtherPC (black) bilayer. The cartoons indicate the membrane region considered for analysis.

(B) Depletion-enrichment map of EtherPC in both cytosolic and luminal leaflet in POPC:EtherPC 85:15 bilayers. The map is obtained as average over 8 replicas.

(C) Depletion-enrichment (D-E) factor for EtherPC in both cytosolic and luminal leaflets in different systems.

(D) D-E map of EtherPC in the luminal leaflet in POPC:EtherPC 85:15 bilayers. The map is obtained as average over 8 replicas.

(E) D-E factor for EtherPC in the luminal leaflet in different systems.

See also Figure S5 and Data S4.

heterogeneity of protein expression within the cell population, we used a high-content automated microscope for image acquisition, and we selected cells within a restricted range of fluorescence intensities of the expressed protein through an analysis pipeline (Figure S3) in an unbiased and consistent way across conditions.

As a proof of concept, we knocked down the p24 protein (TMED2), and we saw no export of GPI-AP even 45 min after the addition of biotin (Figures 5C, 5D, and S4), showing that TMED2 is required for ER exit of GPI-AP in mammalian cells. This is consistent with the existing literature and with p24 function as receptors of GPI-AP in yeast for incorporation in COPII carriers [27, 48, 49].

When we quantified the arrival of GPI-AP to the Golgi at different time points in SL-depleted and EL-depleted cells, we found that 10 min after biotin addition, the amount of GFP-GPI localized at the Golgi was higher under those conditions when compared to control cells (Figures 5E and 5F), suggesting that these lipid changes caused an acceleration of the transport. Moreover, this effect was cumulative if the cells were subjected to both conditions (SL and EL depletion) at the same time, a situation under which cell viability is compromised (Figures 1D and 1H). These experiments measuring ER to Golgi transport of GPI-AP suggest that one of the molecular functions of EL in membranes could be to regulate the selective anterograde transport of GPI-AP (Figures 5E and 5F). They also show that regulation of the kinetics of GPI-AP export from the ER is a conserved function of both SL and EL, although the fact that their effects are additive shows that their functions are not completely redundant. In yeast, it has been shown that GPI-APs, which are Cer-based, leave the ER in distinct COPII vesicles with a particular coat protein composition [50–52]. Similarly, we hypothesize that, in mammalian cells, the presence of ether lipids as part of the GPI anchor and the selective enrichment of ether PC at these sites, close to p24 proteins, could also be a mechanism to facilitate the specific recruitment of GPI-APs and probably separate them from other proteins or lipids that either do not leave the ER or that do it by carrier vesicles with different protein and lipid compositions.

Ether Lipids Are Selectively Enriched around the Luminal Side of the Transmembrane Domain (TMD) of p24

To examine a putative interaction between EL and the TMD of p24, which is one component of our hypothesis, we performed MD simulations following the protocol previously used by Contreras et al. [30] to investigate the interaction between SM C18 and p24. To do so, we tested the interactions of ether PC with p24 TMD in systems containing mixtures of POPC and ether PC lipids (Figure 6A). To identify whether p24 has a specific preference for

EL, we first computed the 2D lateral density of ether PC lipids from the average of 8 independent 1-μs-long MD simulations in 85:15 POPC:ether PC lipid mixtures in the presence of p24 (Figure 6B). Interestingly, the enrichment-depletion map obtained from the 2D lateral density shows that ELs are enriched around the TM helix of p24, albeit only moderately (Figure 6B).

To further quantify the preference of the TM domain of p24 for ether lipids, we explicitly computed the enrichment-depletion index of EL [53] by analyzing lipid-protein contacts along the MD trajectory (Figure 6C). In short, values above 1 indicate enrichment of the given lipid species, although values below 1 indicate depletion. Our data show that, when ELs are present at low concentration, the observed enrichment is not statistically significant and that SLs (SM C18) compete with EL for the binding to p24 (Figure 6C). However, increasing the concentration of ELs in the bilayer results in significant enrichment of ELs around p24, thus mimicking a condition that is more likely to exist under physiological conditions due to the relative amounts of these two lipids in cells (Figure 6C). Of note, the low signal-to-noise ratio is due to a huge replica-to-replica variability, even if the contact fractions show convergence of lipid-protein contacts (Figure S5). Taken together, these data suggest that another possible common function of a particular SM (C18 n-acyl chain) and ether PC is that both seem to bind to and regulate the function of the p24 complex, which is involved in bidirectional vesicular transport in the early secretory pathway [30].

Because the ether moiety of GPI-AP is embedded in the luminal side of the ER, we next investigated whether ELs interact differently with the luminal and the cytosolic part of the TMD of p24. Strikingly, analysis of the enrichment-depletion map (Figure 6D) as well as of the enrichment-depletion factors (Figure 6E) show a more pronounced enrichment of EL around the luminal part of p24. Our results, although consistent with the mechanism for SM binding to p24 previously shown, where only one molecule of SM C18 interacts with the SL binding domain of p24 at a given time, strongly suggest a different role for ether PC when compared to SM C18. SM C18 binds to selected residues of the TMD of p24 in the cytosolic leaflet of the membrane, although ether PC provides a more structural and scaffolding role around the p24 TMD in the luminal leaflet of the membrane.

Our results support a model where different binding mechanisms could be compatible with the proposed dual function of p24 proteins in the secretory pathway. EL would help to organize the selective anterograde transport of GPI-AP, although SL would be required for regulation of COPI-dependent retrograde transport back to the ER. Altogether, the maintenance of the proper levels of these two lipid classes would help maintain the homeostasis of the p24 complex trafficking cycle.

Conclusions

Using a genome-wide screening and lipidomics approach, we identified a number of cellular functions that become essential when SLs are depleted. Many of these concern other lipid synthesis pathways, including cholesterol, fatty acid elongation, and ether lipid synthesis, but we also identified several members involved in the early secretory pathway. Our lipidomics experiments monitored an adaptation to SL depletion that has revealed a genetic interaction and a metabolic co-regulation of EL and SL, suggesting common functions for these two lipid classes. In addition, we found multiple lines of evidence pointing to a specific role of both lipid classes in controlling p24-mediated transport in the early secretory pathway. First, knockdown of p24 proteins (TMED2 and TMED10) renders cells hypersensitive to SL depletion. Second, lipidomic analysis of EL-deficient cells shows a concurrent decrease in SM C18 levels, which is known to specifically regulate p24 ER-to-Golgi cycling. Third, high-content microscopy shows that depletion of both SL and EL impacts transport of GPI-AP between ER and Golgi. Finally, MD simulations validate a molecular crosstalk between both lipid classes and p24 TMD. Together, our data highlight a new role for lipids as direct regulators of intracellular transport and suggest that the lipid diversity found in eukaryotic cells exists in part to ensure the homeostasis of the secretory pathway.

Our results also confirm that, even though major aspects of the secretory pathway are conserved between yeast and human, some regulatory components, like lipids and, as a consequence, lipid-protein interactions, have been modified and have undergone convergent evolution to meet the needs of each organism. ELs are very abundant lipids in mammalian cells, although they seem to be absent from fungi and plants. In yeast, Cer is used for the remodeling of the GPI anchor although ELs have been selected to perform this function in mammalian cells. We propose that the basis for this selection is related to the shared physico-chemical aspects of these lipids and the effects they exert on membranes.

STAR★METHODS

Detailed methods are provided in the online version of this paper and include the following:

- KEY RESOURCES TABLE
- RESOURCE AVAILABILITY
  - Lead Contact
  - Materials Availability
  - Data and Code Availability
- EXPERIMENTAL MODEL AND SUBJECT DETAILS
  - Cell lines
- METHOD DETAILS
  - Cell Counting
  - siRNA transfection
  - DNA transfection
  - Serum de-lipidation
  - MTT assay
  - CRISPRi screen
  - Gene ontology analysis
  - Chemical synthesis of ether PC
  - Lipid extraction
  - Glycerophospholipid and sphingolipid detection on a triple quadrupole TSQ Vantage (ThermoFischer Scientific)
  - Automated fluorescence light microscopy
  - Retention using selective hooks (RUSH)
  - Giant unilamellar vesicle (GUV) formation and imaging
  - Fluorescence lifetime measurements
  - Molecular dynamics simulations
  - RNA extraction and qPCR
- QUANTIFICATION AND STATISTICAL ANALYSIS

SUPPLEMENTAL INFORMATION

ACKNOWLEDGMENTS

AUTHOR CONTRIBUTIONS

N.J.-R., M.D.L., H.R., and J.S.W. designed the work. N.J.-R. performed most of the experiments with input from H.R., S.V., M.D.L., A.C., and A.R. M.D.L. performed the CRISPRi screen. V.Z. and S.V. performed and analyzed the MD simulations. A.C. and A.R. assisted with the FLIM measurements. N.R.I. assisted with the first RUSH measurements. S.M. provided the FLIPPER-TR. S.F. synthesized the ether PC. N.J.-R. and H.R. wrote the manuscript with input from co-authors.

DECLARATION OF INTERESTS

REFERENCES

1. Harayama, T., and Riezman, H. (2018). Understanding the diversity of membrane lipid composition. Nat. Rev. Mol. Cell Biol. 19, 281–296.

2. Lombard, J., López-García, P., and Moreira, D. (2012). The early evolution of lipid membranes and the three domains of life. Nat. Rev. Microbiol. 10, 507–515.

3. Köberlin, M.S., Snijder, B., Heinz, L.X., Baumann, C.L., Fauster, A., Vladimer, G.I., Gavin, A.-C., and Superti-Furga, G. (2015). A conserved circular network of coregulated lipids modulates innate immune responses. Cell 162, 170–183.

4. Hannun, Y.A., and Obeid, L.M. (2018). Sphingolipids and their metabolism in physiology and disease. Nat. Rev. Mol. Cell Biol. 19, 175–191.

5. Goñi, F.M., and Alonso, A. (2006). Biophysics of sphingolipids I. Membrane properties of sphingosine, ceramides and other simple sphingolipids. Biochim. Biophys. Acta 1758, 1902–1921.

6. Bruce, C.R., Risis, S., Babb, J.R., Yang, C., Kowalski, G.M., Selathurai, A., Lee-Young, R.S., Weir, J.M., Yoshioka, K., Takuwa, Y., et al. (2012). Overexpression of sphingosine kinase 1 prevents ceramide accumulation and ameliorates muscle insulin resistance in high-fat diet-fed mice. Diabetes 61, 3148–3155.

7. Ogretmen, B., and Hannun, Y.A. (2004). Biologically active sphingolipids in cancer pathogenesis and treatment. Nat. Rev. Cancer 4, 604–616.

8. Maceyka, M., and Spiegel, S. (2014). Sphingolipid metabolites in inflammatory disease. Nature 510, 58–67.

9. Knudson, A.G., and Kaplan, W.D. (1962). Genetics of the sphingolipidoses. In Cerebral Sphingolipidoses: A Symposium on Tay-Sach's Disease and Allied Disorders, S.M. Aronson, and B.W. Volk, eds. (Academic), pp. 395–411.

10. Penno, A., Reilly, M.M., Houlden, H., Laurá, M., Rentsch, K., Niederkofler, V., Stoeckli, E.T., Nicholson, G., Eichler, F., Brown, R.H., Jr., et al. (2010). Hereditary sensory neuropathy type 1 is caused by the accumulation of two neurotoxic sphingolipids. J. Biol. Chem. 285, 11178–11187.

11. Lovric, S., Goncalves, S., Gee, H.Y., Oskouian, B., Srinivas, H., Choi, W.I., Shril, S., Ashraf, S., Tan, W., Rao, J., et al. (2017). Mutations in sphingosine-1-phosphate lyase cause nephrosis with ichthyosis and adrenal insufficiency. J. Clin. Invest. 127, 912–928.

12. Artetxe, I., Ugarte-Uribe, B., Gil, D., Valle, M., Alonso, A., García-Sáez, A.J., and Goñi, F.M. (2017). Does ceramide form channels? The ceramide-induced membrane permeabilization mechanism. Biophys. J. 113, 860–868.

13. Montes, L.R., Ruiz-Argüello, M.B., Goñi, F.M., and Alonso, A. (2002). Membrane restructuring via ceramide results in enhanced solute efflux. J. Biol. Chem. 277, 11788–11794.

14. Contreras, F.-X., Basañez, G., Alonso, A., Herrmann, A., and Goñi, F.M. (2005). Asymmetric addition of ceramides but not dihydroceramides promotes transbilayer (flip-flop) lipid motion in membranes. Biophys. J. 88, 348–359.

15. Stancevic, B., and Kolesnick, R. (2010). Ceramide-rich platforms in transmembrane signaling. FEBS Lett. 584, 1728–1740.

16. Dressler, K.A., Mathias, S., and Kolesnick, R.N. (1992). Tumor necrosis factor-alpha activates the sphingomyelin signal transduction pathway in a cell-free system. Science 255, 1715–1718.

17. Slotte, J.P. (1999). Sphingomyelin-cholesterol interactions in biological and model membranes. Chem. Phys. Lipids 102, 13–27.

18. Sassa, T., Hirayama, T., and Kihara, A. (2016). Enzyme activities of the ceramide synthases CERS2–6 are regulated by phosphorylation in the C-terminal region. J. Biol. Chem. 291, 7477–7487.

19. Fresques, T., Niles, B., Aronova, S., Mogri, H., Rakhshandehroo, T., and Powers, T. (2015). Regulation of ceramide synthase by casein kinase 2-dependent phosphorylation in Saccharomyces cerevisiae. J. Biol. Chem. 290, 1395–1403.

20. Muir, A., Ramachandran, S., Roelants, F.M., Timmons, G., and Thorner, J. (2014). TORC2-dependent protein kinase Ypk1 phosphorylates ceramide synthase to stimulate synthesis of complex sphingolipids. eLife 3, e03779.

21. Breslow, D.K., Collins, S.R., Bodenmiller, B., Aebersold, R., Simons, K., Shevchenko, A., Ejsing, C.S., and Weissman, J.S. (2010). Orm family proteins mediate sphingolipid homeostasis. Nature 463, 1048–1053.

22. Siow, D.L., and Wattenberg, B.W. (2012). Mammalian ORMDL proteins mediate the feedback response in ceramide biosynthesis. J. Biol. Chem. 287, 40198–40204.

23. Jiménez-Rojo, N., and Riezman, H. (2019). On the road to unraveling the molecular functions of ether lipids. FEBS Lett. 593, 2378–2389.

24. Kanzawa, N., Maeda, Y., Ogiso, H., Murakami, Y., Taguchi, R., and Kinoshita, T. (2009). Peroxisome dependency of alkyl-containing GPI-anchor biosynthesis in the endoplasmic reticulum. Proc. Natl. Acad. Sci. USA 106, 17711–17716.

25. Fujita, M., and Kinoshita, T. (2012). GPI-anchor remodeling: potential functions of GPI-anchors in intracellular trafficking and membrane dynamics. Biochim. Biophys. Acta 1821, 1050–1058.

26. Castillon, G.A., Aguilera-Romero, A., Manzano-Lopez, J., Epstein, S., Kajiwara, K., Funato, K., Watanabe, R., Riezman, H., and Muñiz, M. (2011). The yeast p24 complex regulates GPI-anchored protein transport and quality control by monitoring anchor remodeling. Mol. Biol. Cell 22, 2924–2936.

27. Muñiz, M., Nuoffer, C., Hauri, H.-P., and Riezman, H. (2000). The Emp24 complex recruits a specific cargo molecule into endoplasmic reticulum-derived vesicles. J. Cell Biol. *148*, 925–930.

28. Aguilera-Romero, A., Kaminska, J., Spang, A., Riezman, H., and Muñiz, M. (2008). The yeast p24 complex is required for the formation of COPI retrograde transport vesicles from the Golgi apparatus. J. Cell Biol. *180*, 713–720.

29. Reinhard, C., Schweikert, M., Wieland, F.T., and Nickel, W. (2003). Functional reconstitution of COPI coat assembly and disassembly using chemically defined components. Proc. Natl. Acad. Sci. USA *100*, 8253–8257.

30. Contreras, F.X., Ernst, A.M., Haberkant, P., Björkholm, P., Lindahl, E., Gönen, B., Tischer, C., Elofsson, A., von Heijne, G., Thiele, C., et al. (2012). Molecular recognition of a single sphingolipid species by a protein's transmembrane domain. Nature *481*, 525–529.

31. Hanada, K., Nishijima, M., Kiso, M., Hasegawa, A., Fujita, S., Ogawa, T., and Akamatsu, Y. (1992). Sphingolipids are essential for the growth of Chinese hamster ovary cells. Restoration of the growth of a mutant defective in sphingoid base biosynthesis by exogenous sphingolipids. J. Biol. Chem. *267*, 23527–23533.

32. Gilbert, L.A., Horlbeck, M.A., Adamson, B., Villalta, J.E., Chen, Y., Whitehead, E.H., Guimaraes, C., Panning, B., Ploegh, H.L., Bassik, M.C., et al. (2014). Genome-scale CRISPR-mediated control of gene repression and activation. Cell *159*, 647–661.

33. Bassik, M.C., Kampmann, M., Lebbink, R.J., Wang, S., Hein, M.Y., Poser, I., Weibezahn, J., Horlbeck, M.A., Chen, S., Mann, M., et al. (2013). A systematic mammalian genetic interaction map reveals pathways underlying ricin susceptibility. Cell *152*, 909–922.

34. Guan, X.L., Souza, C.M., Pichler, H., Dewhurst, G., Schaad, O., Kajiwara, K., Wakabayashi, H., Ivanova, T., Castillon, G.A., Piccolis, M., et al. (2009). Functional interactions between sphingolipids and sterols in biological membranes regulating cell physiology. Mol. Biol. Cell *20*, 2083–2095.

35. Lusis, A.J., Rajavashisth, T.B., and Klisak, L. (1989). Identification of a zinc finger protein that binds to the sterol regulatory element. Science *245*, 640–643.

36. Capasso, S., Sticco, L., Rizzo, R., Pirozzi, M., Russo, D., Dathan, N.A., Campelo, F., van Galen, J., Hölttä-Vuori, M., Turacchio, G., et al. (2017). Sphingolipid metabolic flow controls phosphoinositide turnover at the *trans*-Golgi network. EMBO J. *36*, 1736–1754.

37. Düwel, M., and Ungewickell, E.J. (2006). Clathrin-dependent association of CVAK104 with endosomes and the trans-Golgi network. Mol. Biol. Cell *17*, 4513–4525.

38. Saito, K., Yamashiro, K., Ichikawa, Y., Erlmann, P., Kontani, K., Malhotra, V., and Katada, T. (2011). cTAGE5 mediates collagen secretion through interaction with TANGO1 at endoplasmic reticulum exit sites. Mol. Biol. Cell *22*, 2301–2308.

39. Myllyharju, J., and Kivirikko, K.I. (2001). Collagens and collagen-related diseases. Ann. Med. *33*, 7–21.

40. Malhotra, V., and Erlmann, P. (2015). The pathway of collagen secretion. Annu. Rev. Cell Dev. Biol. *31*, 109–124.

41. Kurbatova, E., Otzen, M., and van der Klei, I.J. (2009). p24 proteins play a role in peroxisome proliferation in yeast. FEBS Lett. *583*, 3175–3180.

42. Melero, A., Chiaruttini, N., Karashima, T., Riezman, I., Funato, K., Barlowe, C., Riezman, H., and Roux, A. (2018). Lysophospholipids facilitate COPII vesicle formation. Curr. Biol. *28*, 1950–1958.e6.

43. Reggiori, F., Canivenc-Gansel, E., and Conzelmann, A. (1997). Lipid remodeling leads to the introduction and exchange of defined ceramides on GPI proteins in the ER and Golgi of Saccharomyces cerevisiae. EMBO J. *16*, 3506–3518.

44. Kanzawa, N., Shimozawa, N., Wanders, R.J., Ikeda, K., Murakami, Y., Waterham, H.R., Mukai, S., Fujita, M., Maeda, Y., Taguchi, R., et al. (2012). Defective lipid remodeling of GPI anchors in peroxisomal disorders, Zellweger syndrome, and rhizomelic chondrodysplasia punctata. J. Lipid Res. *53*, 653–663.

45. Colom, A., Derivery, E., Soleimanpour, S., Tomba, C., Molin, M.D., Sakai, N., González-Gaitán, M., Matile, S., and Roux, A. (2018). A fluorescent membrane tension probe. Nat. Chem. *10*, 1118–1125.

46. Dal Molin, M., Verolet, Q., Colom, A., Letrun, R., Derivery, E., Gonzalez-Gaitan, M., Vauthey, E., Roux, A., Sakai, N., and Matile, S. (2015). Fluorescent flippers for mechanosensitive membrane probes. J. Am. Chem. Soc. *137*, 568–571.

47. Boncompain, G., Divoux, S., Gareil, N., de Forges, H., Lescure, A., Latreche, L., Mercanti, V., Jollivet, F., Raposo, G., and Perez, F. (2012). Synchronization of secretory protein traffic in populations of cells. Nat. Methods *9*, 493–498.

48. Fujita, M., Watanabe, R., Jaensch, N., Romanova-Michaelides, M., Satoh, T., Kato, M., Riezman, H., Yamaguchi, Y., Maeda, Y., and Kinoshita, T. (2011). Sorting of GPI-anchored proteins into ER exit sites by p24 proteins is dependent on remodeled GPI. J. Cell Biol. *194*, 61–75.

49. Takida, S., Maeda, Y., and Kinoshita, T. (2008). Mammalian GPI-anchored proteins require p24 proteins for their efficient transport from the ER to the plasma membrane. Biochem. J. *409*, 555–562.

50. Castillon, G.A., Watanabe, R., Taylor, M., Schwabe, T.M., and Riezman, H. (2009). Concentration of GPI-anchored proteins upon ER exit in yeast. Traffic *10*, 186–200.

51. Manzano-Lopez, J., Perez-Linero, A.M., Aguilera-Romero, A., Martin, M.E., Okano, T., Silva, D.V., Seeberger, P.H., Riezman, H., Funato, K., Goder, V., et al. (2015). COPII coat composition is actively regulated by luminal cargo maturation. Curr. Biol. *25*, 152–162.

52. Muñiz, M., Morsomme, P., and Riezman, H. (2001). Protein sorting upon exit from the endoplasmic reticulum. Cell *104*, 313–320.

53. Corradi, V., Mendez-Villuendas, E., Ingólfsson, H.I., Gu, R.X., Siuda, I., Melo, M.N., Moussatova, A., DeGagné, L.J., Sejdiu, B.I., Singh, G., et al. (2018). Lipid-protein interactions are unique fingerprints for membrane proteins. ACS Cent. Sci. *4*, 709–717.

54. Gilbert, L.A., Larson, M.H., Morsut, L., Liu, Z., Brar, G.A., Torres, S.E., Stern-Ginossar, N., Brandman, O., Whitehead, E.H., Doudna, J.A., et al. (2013). CRISPR-mediated modular RNA-guided regulation of transcription in eukaryotes. Cell *154*, 442–451.

55. Mi, H., Muruganujan, A., Ebert, D., Huang, X., and Thomas, P.D. (2019). PANTHER version 14: more genomes, a new PANTHER GO-slim and improvements in enrichment analysis tools. Nucleic Acids Res. *47* (D1), D419–D426.

56. Klauda, J.B., Venable, R.M., Freites, J.A., O'Connor, J.W., Tobias, D.J., Mondragon-Ramirez, C., Vorobyov, I., MacKerell, A.D., Jr., and Pastor, R.W. (2010). Update of the CHARMM all-atom additive force field for lipids: validation on six lipid types. J. Phys. Chem. B *114*, 7830–7843.

57. Humphrey, W., Dalke, A., and Schulten, K. (1996). VMD: visual molecular dynamics. J. Mol. Graph. *14*, 33–38, 27–28.

58. Blasi, E., Barluzzi, R., Bocchini, V., Mazzolla, R., and Bistoni, F. (1990). Immortalization of murine microglial cells by a v-raf/v-myc carrying retrovirus. J. Neuroimmunol. *27*, 229–237.

59. Horlbeck, M.A., Gilbert, L.A., Villalta, J.E., Adamson, B., Pak, R.A., Chen, Y., Fields, A.P., Park, C.Y., Corn, J.E., Kampmann, M., and Weissman, J.S. (2016). Compact and highly active next-generation libraries for CRISPR-mediated gene repression and activation. eLife *5*, e19760.

60. Jassal, B., Matthews, L., Viteri, G., Gong, C., Lorente, P., Fabregat, A., Sidiropoulos, K., Cook, J., Gillespie, M., Haw, R., et al. (2020). The reactome pathway knowledgebase. Nucleic Acids Res. *48* (D1), D498–D503.

61. Guri, Y., Colombi, M., Dazert, E., Hindupur, S.K., Roszik, J., Moes, S., Jenoe, P., Heim, M.H., Riezman, I., Riezman, H., and Hall, M.N. (2017). mTORC2 promotes tumorigenesis via lipid synthesis. Cancer Cell *32*, 807–823.e12.

62. Broniec, A., Klosinski, R., Pawlak, A., Wrona-Krol, M., Thompson, D., and Sarna, T. (2011). Interactions of plasmalogens and their diacyl analogs with singlet oxygen in selected model systems. Free Radic. Biol. Med. *50*, 892–898.

63. Horger, K.S., Estes, D.J., Capone, R., and Mayer, M. (2009). Films of agarose enable rapid formation of giant liposomes in solutions of physiologic ionic strength. J. Am. Chem. Soc. *131*, 1810–1819.

64. Fidorra, M., Garcia, A., Ipsen, J.H., Härtel, S., and Bagatolli, L.A. (2009). Lipid domains in giant unilamellar vesicles and their correspondence with equilibrium thermodynamic phases: a quantitative fluorescence microscopy imaging approach. Biochim. Biophys. Acta *1788*, 2142–2149.

65. Roux, A., Koster, G., Lenz, M., Sorre, B., Manneville, J.B., Nassoy, P., and Bassereau, P. (2010). Membrane curvature controls dynamin polymerization. Proc. Natl. Acad. Sci. USA *107*, 4141–4146.

66. Wahl, M., Koberling, F., Patting, M., Rahn, H., and Erdmann, R. (2004). Time-resolved confocal fluorescence imaging and spectrocopy system with single molecule sensitivity and sub-micrometer resolution. Curr. Pharm. Biotechnol. *5*, 299–308.

67. Abraham, M., Hess, B., van der Spoel, D., and Lindahl, E. (2018). GROMACS User Manual Version 2018 (GROMACS).

68. Leonard, A.N., Pastor, R.W., and Klauda, J.B. (2018). Parameterization of the CHARMM all-atom force field for ether lipids and model linear ethers. J. Phys. Chem. B *122*, 6744–6754.

69. Jo, S., Kim, T., and Im, W. (2007). Automated builder and database of protein/membrane complexes for molecular dynamics simulations. PLoS ONE *2*, e880.

70. Jo, S., Kim, T., Iyer, V.G., and Im, W. (2008). CHARMM-GUI: a web-based graphical user interface for CHARMM. J. Comput. Chem. *29*, 1859–1865.

71. Lee, J., Cheng, X., Swails, J.M., Yeom, M.S., Eastman, P.K., Lemkul, J.A., Wei, S., Buckner, J., Jeong, J.C., Qi, Y., et al. (2016). CHARMM-GUI input generator for NAMD, GROMACS, AMBER, OpenMM, and CHARMM/OpenMM simulations using the CHARMM36 additive force field. J. Chem. Theory Comput. *12*, 405–413.

72. Parrinello, M., and Rahman, A. (1981). Polymorphic transitions in single crystals: a new molecular dynamics method. J. Appl. Phys. *52*, 7182–7190.

73. Berendsen, H.J.C., Postma, J.P.M., van Gunsteren, W.F., DiNola, A., and Haak, J.R. (1984). Molecular dynamics with coupling to an external bath. J. Chem. Phys. *81*, 3684–3690.

74. Nosé, S. (1984). A molecular dynamics method for simulations in the canonical ensemble. Mol. Phys. *52*, 255–268.

75. Páll, S., and Hess, B. (2013). A flexible algorithm for calculating pair interactions on SIMD architectures. Comput. Phys. Commun. *184*, 2641–2650.

STAR★METHODS

KEY RESOURCES TABLE

REAGENT or RESOURCE	SOURCE	IDENTIFIER
Antibodies		
Mouse mononclonal anti-GM130	BD Biosciences	Cat# 610822
		RRID: AB_398141
Alexa Fluor® 647-AffiniPure Donkey Anti-Mouse IgG (H+L)	Jackson ImmunoResearch	Cat# 715-605-150
		RRID: AB_2340862
Chemicals, Peptides, and Recombinant Proteins		
Myriocin from *Mircelia Sterilia*	Merck (Sigma-Aldrich)	Cat# M1177
		CAS: 35891-70-4
Ceramide 24:1	Avanti Polar Lipids	Cat# 860525
		CAS: 54164-50-0
1-palmitoyl-2-oleoyl-glycero-3-phosphocholine (POPC)	Avanti Polar Lipids	Cat# 850457
		CAS: 26853-31-6
1-O-hexadecyl-2-hydroxy-sn-glycero-3-phosphocholine(Lyso PAF)	Avanti Polar Lipids	Cat #878119
		CAS: 52691-62-0
1-O-hexadecyl-2-oleoyl-sn-glycero-3-phosphocholine (Ether PC)	This study	N/A
Opti-MEM, Reduced Serum Medium	Thermo Fisher Scientific (GIBCO life technologies)	Cat# 31985047
DMEM, GLUTAMAX, pyruvate, high glucose (4.5 g/L)	Thermo Fisher Scientific (GIBCO life technologies)	Cat# 31966047
DMEM, high glucose (4.5 g/L), no phenol red	Thermo Fisher Scientific (GIBCO life technologies)	Cat# 21063029
DPBS (x1)	Thermo Fisher Scientific (GIBCO life technologies)	Cat# 14190-094
RPMI 1640 Medium, HEPES	Thermo Fisher Scientific (GIBCO life technologies)	Cat# 42401018
Fetal Bovine Serum (FCS)	Thermo Fisher Scientific (GIBCO life technologies)	Cat# 10270106
		Lot# 41G1840K
Fetal Bovine Serum (FBS), for K562 culture	GE Life Sciences	Cat# SH30071.03
		Lot# AZA180864
Lipid Removal Adsorbent (LRA)	SIGMA-ALDRICH-FLUKA	Cat# 13358-U
Penicillin/Streptomicin	Thermo Fisher Scientific (GIBCO life technologies)	Cat# 10378016
Trypsin-EDTA	Thermo Fisher Scientific (GIBCO life technologies	Cat# 25300054
Lipofectamine RNAiMAX Transfection Reagent	Thermo Fisher Scientific	Cat# 13778075
*Trans*IT-X2® Dynamic Delivery System	Mirus Bio	Cat# MIR 6003
D-Biotin	Thermo Fisher Scientific	Cat# B1595
BSA	Merck (Sigma-Aldrich)	Cat# A6003-5G
MTT (3-(4,5-Dimethylthiazol-2-yl)-2,5-Diphenyltetrazolium Bromide)	Thermo Fisher Scientific	Cat# M6494
		CAS: 2348-71-2
Agarose (Ultra-low gelling temperature)	Merck (Sigma-Aldrich)	Cat# A2576
Dimethyl sulfoxide (DMSO) (Cell culture grade)	AppliChem	Cat# A3672
Standard (lipidomics): DLPC 12:0-12:0 PC (0.4 nmole/dish)	Avanti	Cat# 850335
Standard (lipidomics): PE31:1 17:0-14:1 PE (1 nmole/dish)	Avanti	Cat# LM-1104

(*Continued on next page*)

http://doc.rero.ch

Continued

REAGENT or RESOURCE	SOURCE	IDENTIFIER
Standard (lipidomics): PI31:1 17:0-14:1 PI (1 nmole/dish)	Avanti	Cat# LM-1504
Standard (lipidomics): PS31:1 17:0-14:1 PS (3.3 nmole/dish)	Avanti	Cat# LM-1304
Standard (lipidomics): CL56:0 14:0 Cardiolipin (0.7 nmole/dish)	Avanti	Cat# 710332
Standard (lipidomics): C17Cer C17 Ceramide d18:1-17:0) (2.5 nmole/dish)	Avanti	Cat# 860517
Standard (lipidomics): C8GC C8 Glucosyl(B) Ceramide (d18:1-8:0) (0.5 nmole/dish)	Avanti	Cat# 860540
Standard (lipidomics): C12SM 12:0 SM (d18:1-12:0) (0.1 nmole/dish)	Avanti	Cat# 860583
18:1 Liss Rhod PE (1,2-dioleoyl-sn-glycero-3-phosphoethanolamine-N-(lissamine rhodamine B sulfonyl) (ammonium salt))	Avanti	Cat# 810150C
D(+)-Sucrose for molecular biology	AppliChem	Cat# A2211
DMAP (4-Dimethylaminopyridine)	SIGMA-ALDRICH	Cat# 820499
		CAS: 1122-58-3
DIPEA (N,N-Diisopropylethylamine)	SIGMA-ALDRICH	Cat# 387649
		CAS: 7087-68-5
Oleoyl Chloride	SIGMA-ALDRICH	Cat# 367850
		CAS: 112-77-6
Simvastatin	SIGMA-ALDRICH	Cat # S6196
		CAS: 79902-63-9
Critical Commercial Assays		
RNeasy MiniKit	Quiagen	Cat# 74104
PureLink™ Midiprep kit	Invitrogen	Cat# K210015
SsoAdvanced Universal SYBR® Green Supermix	Bio-rad	Cat# 172-5274
dNTP Set (100 mM)	Thermo Fisher Scientific	Cat# 10297-018
Superscript II™ Reverse transcriptase	Invitrogen	Cat# 18064014
Deposited Data		
Raw sequencing data	This paper	https://www.ncbi.nlm.nih.gov/geo/query/acc.cgi?acc=GSE154045
Raw lipidomics data	This paper	http://doi.org/10.26037/yareta:bkiubi7cczhgbjkkzx2h6mpzya
Experimental Models: Cell Lines		
Calu-6	ATCC®	Cat# HTB-56
BV2	[54]	N/A
K562 dCas9-Krab	[32]	N/A
Oligonucleotides		
siPOOL-TMED2 (Gene ID: 10959)	siTOOLs BIOTECH, Planegg, Germany	N/A
siPOOL-SMPD3 (Gene ID: 55512)	siTOOLs BIOTECH, Planegg, Germany	N/A
siPOOL-SMPD1 (Gene ID: 6609)	siTOOLs BIOTECH, Planegg, Germany	N/A
CRISPRi gRNA pooled genome-wide library	[32]	Addgene library #62217
Recombinant DNA		
Str-KDEL_SBP-EGFP-GPI	[48]	Addgene Plasmid #65294

Continued		
REAGENT or RESOURCE	SOURCE	IDENTIFIER
Software and Algorithms		
Weissman laboratory CRISPRi screen analysis in Python	[55]	https://github.com/mhorlbeck/ScreenProcessing
GROMACS	[56]	http://manual.gromacs.org/documentation/
VMD	7[57]	https://www.ks.uiuc.edu/Development/Download/download.cgi?PackageName=VMD
MATLAB	MathWorks	https://ch.mathworks.com/downloads/web_downloads/?s_iid=hp_ff_t_downloads

RESOURCE AVAILABILITY

Lead Contact
Further information and requests for resources and reagents should be directed to and will be fulfilled by the Lead Contact, Prof. Howard Riezman. (Howard.Riezman@unige.ch).

Materials Availability
This study did not generate new unique reagents.

Data and Code Availability
Sequencing data was uploaded to GEO under accession number GSE154045.
  Mass Spectrometry dataset: https://doi.org/10.26037/yareta:bkiubi7cczhgbjkkzx2h6mpzya

EXPERIMENTAL MODEL AND SUBJECT DETAILS

Cell lines
K562 cells were purchased from ATCC (ATCC® HTB-56) and cultured as shown in the section regarding the CRISPRi screen. HeLa (Kyoto) cells were a gift from Anthony Hyman group (MPI-CBG) and were cultured at $37°C$ and 5% CO_2 in Dulbecco's Modified Eagle Medium (Cat# 31966047, DMEM, GIBCO™) with 4.5 g/L glucose, supplemented with 10% delipidated fetal calf serum (FCS, Hyclone) and 1% Pen/Strep (Cat# 10378016, GIBCO™). BV2 cells were provided by Prof. Thierry Soldati (University of Geneva) [58] and Calu-6 cells were purchased from ATCC (ATCC® HTB-56). Both cell lines were cultured in the same conditions as HeLa cells.

METHOD DETAILS

Cell Counting
The number of cells was determined using a Countess II FL Automated Cell Counter and Countess Cell Counting Chamber Slides which include the trypan blue solution (Thermo Fisher Scientific).

siRNA transfection
Transfections with siRNAs were performed using Lipofectamine RNAiMax (Cat# 13778075, Thermo Fisher Scientific) using the supplier's instructions, for 3 days, if other conditions are not specified. The siRNA solutions were diluted using Opti-MEM® (Cat# 31985047). The siRNAs used in this work were: siPOOL-TMED2 (Gene ID: 10959), siPOOL-SMPD1 (Gene ID: 6609), siPOOL-SMPD3 (Gene ID: 55512), and siPOOL non-coding (nc) siRNA (siTOOLs BIOTECH, Planegg, Germany).

DNA transfection
TransIT-X2® Dynamic Delivery System (Mirus Bio) was used to transfect plasmid DNA. Str-KDEL_SBP-EGFP-GPI construct was a gift from Franck Perez (Addgene plasmid #65294).

Serum de-lipidation
Serum de-lipidation was achieved using lipid removal adsorbent (LRA, MilliporeSigma #13358-U). 500mL of fetal bovine serum (FBS, HyClone GE Life Sciences) was incubated overnight with 25 g LRA resin under constant rotation at $4°C$. Resin particles were then decanted by centrifugation (first spin for 5min at 2,000xg for bulk removal, second spin at 27,000xg for fine particle removal). FBS pH was adjusted to 7.4 with NaOH and filter-sterilized using a 0.2μm membrane twice.

MTT assay
The MTT(3-[4,5-dimethylthiazol-2-yl]-2,5- diphenyltetrazolium bromide; thiazolyl blue) (Cat# M6494, Thermo Fisher Scientific) assays were performed in 96-well black/clear bottom plates (FALCON®, Corning). MTT was dissolved in Dulbecco's Modified Eagle Medium

without phenol red to a 5 mg/ml stock solution, added to each well to be one-tenth the original culture volume and incubated for 3 to 4 hr. At the end of the incubation period the medium was removed and the dye was solubilized with DMSO: isopropanol (1:1). Absorbance of converted dye is measured at a wavelength of 570 nm with background subtraction at 630–690 nm.

CRISPRi screen

Screens were performed in K562 cells stably expressing a constitutive SFFV-dCas9-BFP-KRAB CRISPRi transcriptional repression construct using lentiviral transduction [54] (Addgene plasmid # 46911). K562 CRISPRi cells were grown in RPMI 1640 HEPES medium supplemented with 10% lipid-depleted FBS and transduced with a genome-wide sgRNA library targeting the transcriptional start site of $\sim$16,000 protein-coding genes as well as 1,000 negative control scrambled sgRNA sequences as in [32](Addgene pooled library # 62217). Each protein-coding gene was targeted by a minimum of 10 unique sgRNA sequences to ensure statistical power, and cell culture was scaled to ensure a minimum representation of 1,000 cells per unique sgRNA at all times. sgRNA-expressing cells were puromycin-selected as in [32], a "time zero" sample was isolated and the cell pool was subsequently split into two parallel 1-l cultures in spinner flasks under constant agitation. One culture was treated with 1μM myriocin (MilliporeSigma #M1177, resuspended a 1mM in DMSO) while a control culture was treated with DMSO. Sphingolipid depletion was insured by myriocin treatment for 6 days, followed by 6 days of recovery in drug-free media. Cells from both cultures were then harvested for bulk genomic DNA extraction, and the sgRNA-encoding regions were then amplified by PCR and sequenced on an Illumina HiSeq-2500 as in [32]. Myriocin-specific phenotypes (ρ) were quantified by comparing the frequency of cells harboring a given sgRNA sequence between the treated and un-treated cultures, while growth phenotypes (γ) were quantified by comparing, within each cultures, sgRNA frequencies between the final cell pools and the "time zero" sample [32, 33]. Bioinformatic analysis was performed as in [59] using publicly available Python scripts (https://github.com/mhorlbeck/ScreenProcessing). Briefly, gene hits were scored based on the average phenotype of the 3 strongest sgRNAs (by absolute value) targeting their TSS using a Mann-Whitney test against the non-targeting control set. For each gene, the myriocin-specific gene phenotype representing resistance to treatment (ρ) was calculated as described in [33], and forms the basis of our analysis. Both growth (γ) and myriocin-specific (ρ) phenotypes for each genes are included in the Data S1.

Gene ontology analysis

Analysis was performed using PANTHER (http://pantherdb.org) [55] and pathway annotations from Reactome v65 [60].

Chemical synthesis of ether PC

To a solution of Lyso-PAF C16 (10.9 mg, 0.023 mmol) in chloroform (1.0 mL), oleoyl chloride (30 μL), DMAP (cat. amount), and DIPEA (40 μL) was added. The reaction mixture was stirred at 55°C for 2 hours. The crude product was directly purified by flash chromatograph (SiO$_2$, first MeOH/DCM (1/10), then MeOH/DCM/H$_2$O (2/1/0.1, v/v)) to yield the product as a solid (13.5 mg, yield: 77%). The reaction and purification were monitored by thin layer chromatograph (TLC) using phosphomolybdic acid (PMA) staining.

Lipid extraction

For lipidomics experiments 3x10^5 cells were seeded in 6 cm dishes and harvested after 3 days of culture in delipidated medium ($\approx 1 \times 10^6$ cells). Lipid extraction was performed using a modified methyl tert-butyl ether (MTBE) protocol [61]. Cells were first washed with cold PBS and scraped off in 500 μl cold PBS on ice. The suspension was transferred to a 2 mL Eppendorf tube and spin down at 3200 rpm for 5 minutes at 4°C. After removing the PBS, samples were stored at -20°C or directly used for further extraction. Then, 360 μL methanol was added and vortexed. A mixture of lipid standards (see Key Resources Table, represented in nmol of lipid per dish/sample) was added and the cells were vortexed for 10 minutes at 4°C using a Cell Disruptor Genie (Scientific Industries, Inc). MTBE (1.2 mL) was then added and the samples were incubated for one hour at room temperature with shaking (750 rpm). Phase separation was induced by adding 200 μL H$_2$O. After 10 min of incubation at RT, the sample was centrifuged at 1000 x g for 10 min (RT). The upper (organic) phase was transferred in a 13 mm screw cap glass tube and the lower phase was extracted with 400 μL artificial upper phase (MTBE/methanol/water (10:3:1.5, v/v)). The two upper phases were combined and the total lipid extract was divided in 3 equal aliquots (one for phospholipids (TL), one for sterols (S) in 2 mL amber vials and one for SL [62] in a 13 mm glass tube) and dried in a Centrivap at 50°C or under a nitrogen flow. The SL aliquot was deacylated to eliminate phospholipids by methylamine treatment (Clarke method). 0.5 mL monomethylamine reagent (MeOH/H2O/n-butanol/Methylamine solution (4:3:1:5 v/v) was added to the dried lipid, followed by sonication (5 min). Samples were then mixed and incubated for one hour at 53°C and dried (as above). The monomethylamine treated lipids were desalted by n-butanol extraction. 300 μL H$_2$O saturated n-butanol was added to the dried lipids. The sample was vortexed, sonicated for 5 min and 150 μL MS grade water was added. The mixture was vortexed thoroughly and centrifuged at 3200 x g for 10 min. The upper phase was transferred in a 2 mL amber vial. The lower phase was extracted twice more with 300 μL H$_2$O saturated n-butanol and the upper phases were combined and dried (as above).

Glycerophospholipid and sphingolipid detection on a triple quadrupole TSQ Vantage (ThermoFischer Scientific)

TL and SL aliquots were resuspended in 250 μL Chloroform/methanol (1:1 v/v) (LC-MS/HPLC GRADE) and sonicated for 5 minutes. The samples were pipetted in a 96 well plate (final volume = 100 μl). The TL were diluted 1:4 in negative mode solvent (Chloroform/Methanol (1:2) + 5mM Ammonium acetate) and 1:10 in positive mode solvent (Chloroform/Methanol/Water (2:7:1 v/v) + 5mM Ammonium Acetate). The SL were diluted 1:10 in positive mode solvent and infused onto the mass spectrometer. Tandem mass spectrometry for the identification and quantification of lipid molecular species was performed using Multiple Reaction Monitoring (MRM) with

a TSQ Vantage Triple Stage Quadrupole Mass Spectrometer (Thermo Fisher Scientific) equipped with a robotic nanoflow ion source, Nanomate HD (Advion Biosciences, Ithaca, NY). The collision energy was optimized for each lipid class. The detection conditions for each lipid class are listed in Table S1. Ceramide species were also quantified with a loss of water in the first quadrupole. Each biological replicate was read in 2 technical replicates (TR). Each TR comprised 3 measurements for each transition. Lipid concentrations were calculated relative to the relevant internal standards and then normalized to the total lipid content of each lipid extract (mol%).

Automated fluorescence light microscopy

For the high content microscopy experiments we used black 96-well imaging plates (cat# 89626, Ibidi). 3000 cells were seeded per well in media containing either the vehicle (MetOH) or 1.5 μM myriocin from a 5 mM stock solution. A reverse transfection has been performed for each siRNA experiment, using lipofectamine RNAimax following manufacturer instructions. After 48 hours of incubation, DNA transfection was performed for another 24 hours. Briefly, the medium from each well was replaced with 120 μL of fresh media added to a 30 μL DNA solution previously diluted in Opti-MEM and mixed with *Trans*IT-X2® Dynamic Delivery System reagent in a 3:1 *Trans*IT-X2 (μL): DNA (μg) ratio.

Retention using selective hooks (RUSH)

In order to synchronize and follow the export of GPI-AP in our cells, we use the RUSH system previously described by Boncompain et al. [47]. Briefly, the GPI construct containing an SBP tag (streptavidin binding protein) and a fluorescent protein (EGFP) is fused to minimal ER hook containing streptavidin and a C-terminal ER retention signal (KDEL, Lys-Asp- Glu-Leu) giving rise to the Str-KDEL_SBP-EGFP-GPI construct that is used for transfection. Once the biotin is added to the cells that are successfully transfected, the reporter (SBP-EGFP-GPI) is released from the ER hook and follows the secretory pathway. Arrival to the Golgi is measured as explained below, following colocalization of the EGFP-GPI construct with GM130, a Golgi resident protein stained first with a primary purified mouse anti- GM130 antibody (Cat# 610822, BD Biosciences) following staining with a secondary Alexa Fluor® 647-AffiniPure Donkey Anti-Mouse IgG (H+L) (Cat# 715-605-150, Jackson ImmunoResearch).

Before the experiment was performed, a solution of biotin was prepared in media at a concentration of 120 μM (40 μM final concentration in each well). Media was replaced in each well by 100 μL of fresh media and the cells were kept in the incubator for at least 30 minutes before the experiment. To start the release of the transfected fluorescent cargo, 50 μL of the biotin solution were added at different time points (45, 30, 15, 10, and 5 minutes). After 45 minutes the plate was fixed using 4% PFA solution and washed using an automated plate washer (BioTek EL406). Cells were then stained as follows: step 1: monoclonal antibody against GM130, 1/500, saponin 0.05%, BSA 1%, in PBS, incubation for 1 h and, step 2: Hoechst 33342 Solution (20 mM) (1/5000), Cy5-labeled secondary antibody against mouse IgG, 1/500, incubation for 30 min. Image acquisition was performed immediately after staining using a ImageXpress® Micro Confocal High-Content Imaging System (Molecular devices) with the 40 × objective. 36 images were captured per well. For image analysis, we used the MetaXpress Custom Module editor software to first segment the image and generate relevant masks (Figure S3). In the first step, individual cells were identified using the staining of the nuclei (Hoechst channel). Next, the Golgi was segmented from the images using the signal coming from the anti-GM130 antibody (Cy5 channel, Figure S3). Properly transfected cells were then selected using those ones with a fluorescence intensity of the cargo (EGFP-GPI) ranging between two specific values, identical through all conditions. Finally, the masks were applied to the original fluorescence images, and different measurements were obtained per cell (e.g., integrated intensity, average intensity and object count). The average intensity value of the fluorescent cargo in the Golgi is used to represent the data. The same imaging and analysis pipelines were applied to all images. Data analysis was with Prism Graph Pad 8.0.

Giant unilamellar vesicle (GUV) formation and imaging

Giant unilamellar vesicles (GUVs) were prepared by the agarose method [63]. All the lipids purchased for this study were from Avanti Polar Lipids, Inc. (Alabaster, AL): Cer 24:1 (Cat# 860525), POPC (Cat# 850457). Stock lipid solutions (2 mg/ml total lipid) were prepared in chloroform: methanol (2:1, v/v) and spread on ultra low gelling agarose (Sigma-Aldrich # A2576) (1%)-coated glass slides. First, the glass slides were dipped in the agarose solution and dried by keeping the slides for 2 h at 30oC or overnight at room temperature. Then the lipid mixtures were spread onto the agarose-coated slides. For GUV formation, a solution of 280mM sucrose was added to each slide and the chambers were placed at the desired temperature, always above the transition temperature of the lipid mixtures. For the confocal microscopy: a home-made chamber was used that allows direct GUV visualization under the microscope [64, 65].

Fluorescence lifetime measurements

FLIM imaging was performed using a Nikon Eclipse Ti A1R microscope equipped with a Time Correlated Single-Photon Counting module from PicoQuant as previously published [45, 66]. Excitation was performed using a pulsed 485nm laser (PicoQuant, LDH-D-C-485) operating at 20 MHz, and emission signal was collected through a bandpass 600/50nm filter using a gated PMA hybrid 40 detector and a TimeHarp 260 PICO board (PicoQuant). SymPhoTime 64 software (PicoQuant) was then used to fit fluorescence decay data (from full images or regions of interest) to a dual exponential model after deconvolution for the instrument response function (measured using the backscattered emission light of a 1 μM fluorescein solution with 4M KI). Data was expressed as means ± standard deviation of the mean. The full width at half-maximum (FWHM) response of the instrument was measured at 176 ps.

Molecular dynamics simulations

Molecular dynamics simulations were run with the GROMACS [67] software using the CHARMM36 force field [56, 68]. The coordinates of p24 TMD were used as described in [30]. The CHARMM GUI *Membrane Builder [69–71]* was used to build systems containing p24 already inserted in the bilayer, with 122 lipids, 50 water/molecules per lipid and ion concentration of 150 mmol/L. The same approach was used to build pure lipid bilayers, with 100 lipids per leaflet and 70 water molecules per lipid. For the systems containing ether PC, as this lipid is not natively present in CHARMM-GUI, lipid bilayers containing SOPC were built and then atom types were modified with an in-house script for conversion to ether PC. The force field parameters for ether PC are provided in Figure S5.

The simulations containing p24 were equilibrated using the CHARMM GUI procedure that involves minimization followed by steps in which positional restraints for lipid head groups and protein backbone are gradually lowered and removed. The systems were minimized using a steepest descent algorithm until reaching a force smaller than 1000 kJ mol^{-1} nm^{-1}. A 175000-step equilibration with a time step increasing from 0.001 to 0.002 ps was run, followed by a 1000 ns production, with a time step of 0.002 ps. In both equilibration and production, pressure was controlled by a Parrinello-Rahman barostat [72] and average pressure was 1 atm, coupled every 5 ps. During equilibration, a Berendsen thermostat [73] was used, while during production temperature was controlled via a Nosé-Hoover thermostat [74], coupled every 1 ps and the target temperature was 310K during the entire run. The lateral *xy* dimensions were coupled, while the *z* dimension was allowed to fluctuate independently. For calculation of non-bonded interactions, the standard procedure provided by the CHARMM-GUI tool was followed [67] fast smooth Particle-Mesh Ewald (SPME) [73] was used for calculations of electrostatics. A cutoff scheme was used for the vdW terms, with a cut-off distance of 1.2 nm and the Verlet cut-off scheme for the force-shift [75], as suggested in http://manual.gromacs.org/documentation/2018/user-guide/force-fields.html.

For systems containing only lipid bilayers the same settings were used, but with a different equilibration protocol: a minimization using a steepest descent algorithm until reaching a force smaller than 700 kJ mol^{-1} nm^{-1} was performed, followed by a 20 ps equilibration with a time step of 0.001 and using a Nosé-Hoover thermostat for temperature control. Finally, productions were run for 200 ns, with a time step of 0.002 ps. Two independent replicas for each lipid compositions (see Table S2) were randomly generated with CHARMM-GUI and run.

For the systems containing both ether PC and p24, for each different lipid composition, 8 independent 1 μs-long replicas were generated using CHARMM-GUI with lipids randomly positioned at the beginning of the run (Table S2).

The number of protein-lipid contacts were calculated using GROMACS tools, defined as contacts within a cutoff of 0.7 nm between the phosphate atom of lipids and the protein. The depletion-enrichment factors were calculated, as in [53] according to the following formula:

$$D - E\ factor = \frac{\left(number\ of\ EtherPC\middle/ number\ of\ total\ lipids\right)_{within\ 0.7\ of\ protein}}{\left(number\ of\ EtherPC\middle/ number\ of\ total\ lipids\right)_{bulk}}$$

The values reported are obtained as average and the error bars as standard error over 8 independent replicas. The statistical significance of the D-E factor was calculated from t test ((average$_{DE\text{-factor}}$-1)/standard error) and P values were computed from a one-tailed distribution against the null-hypothesis (no enrichment).

2D lateral density maps for the systems containing p24 were calculated using GROMACS tools. To obtain an enrichment/depletion map for EtherPC, the density maps of EtherPC was divided by the sum of the maps of EtherPC and POPC and then divided by the concentration of EtherPC in bulk. The same colormap scale has been used, to compare the magnitude of enrichment in different systems.

Hydrogen bonds calculation was performed using GROMACS tools. All the images were rendered using VMD [57] and the graphs created using MATLAB.

RNA extraction and qPCR

Cells were grown in 6 cm dishes. Total RNA extraction was performed using the RNeasy Mini Kit (QIAGEN No: 74104). RNA quantity and purity were controlled using a spectrophotometer: ratios 260/280 (protein contamination) and 260/230 (guanidinium thiocyanate contamination) were greater than or equal to 2.0.

One microgram of RNA was used for cDNA synthesis using the Superscript II (Invitrogen) reverse transcription reaction with random hexamers. qPCR analysis was performed on a CFX Connect Real-Time PCR system using SsoAdvanced Universal SYBR Green supermix (Bio-Rad, Switzerland).

Primers were designed using Primer-BLAST, and sequences were the following (5′- > 3′):

AGPS-forward: GAGTGCAAAGCGCGGAGA.
AGPS reverse: TTCTTGCCGCTTCTTTGGGA.
TATA-binding protein (TBP)-forward: CCGCCGGCTGTTTAACTTC.
TATA-binding protein-reverse: AGAAACAGTGATGCTGGGTCA.

The amplification profile for qPCR was 95°C, 1 min, followed by 40 amplification cycles at 95°C, 10 s, and 60°C, 30 s. The run was completed with the dissociation curve from the start at 65°C to 95°C with 0.5 increments. Data analysis was done with the Bio-Rad

CFX manager software version 3.1. Expression of the target gene was calculated relative to the wild-type condition after normalization to the reference gene TBP. Triple biological replicates and triple technical replicates were analyzed.

QUANTIFICATION AND STATISTICAL ANALYSIS

Statistical analyses and data plotting were performed using Prism Graph Pad 8.0. An unpaired, two tailed, unequal variance t test assuming Gaussian distribution was used to compare between two groups. Data represent mean ± SEM and p values are shown in the figures.